

Effective Buoyancy, Inertial Pressure, and the Mechanical Generation of Boundary Layer Mass Flux by Cold Pools

NADIR JEEVANJEE

Department of Physics, University of California, Berkeley, and Earth Sciences Division, Lawrence Berkeley National Laboratory, Berkeley, California

DAVID M. ROMPS

Department of Earth and Planetary Science, University of California, Berkeley, and Earth Sciences Division, Lawrence Berkeley National Laboratory, Berkeley, California

(Manuscript received 1 December 2014, in final form 13 April 2015)

ABSTRACT

The Davies-Jones formulation of effective buoyancy is used to define inertial and buoyant components of vertical force and to develop an intuition for these components by considering simple cases. This decomposition is applied to the triggering of new boundary layer mass flux by cold pools in a cloud-resolving simulation of radiative-convective equilibrium (RCE). The triggering is found to be dominated by inertial forces, and this is explained by estimating the ratio of the inertial forcing to the buoyancy forcing, which scales as H/h , where H is the characteristic height of the initial downdraft and h is the characteristic height of the mature cold pool's gust front. In a simulation of the transition from shallow to deep convection, the buoyancy forcing plays a dominant role in triggering mass flux in the shallow regime, but the force balance tips in favor of inertial forcing just as precipitation sets in, consistent with the RCE results.

1. Introduction

The initiation of convection is an outstanding and pressing issue in cloud dynamics. Clarification of the mechanisms involved is necessary for the construction of reliable parameterizations, and in particular for reliably “closing” mass flux schemes, which must diagnose cloud-base mass flux in terms of prognostic variables. Many current mass flux schemes, such as the Zhang-McFarlane scheme (Zhang and McFarlane 1995) currently employed in the Community Atmosphere Model (Neale et al. 2013), have closures that rely on uncertain convective time-scale parameters, to which the parent models exhibit considerable sensitivity (Qian et al. 2015; Mishra 2011; Mishra and Srinivasan 2010). Thus, a firm understanding of how convection is initiated is critical for trustworthy convective parameterizations and accurate simulations of global climate.

Though convection can take many forms (e.g., trade cumulus, squall lines, mesoscale convective systems) and is variously influenced by the large-scale environment (e.g., surface temperature gradients, wind shear, and large-scale vertical motion), the mass flux closure problem remains unsolved even in the simple case of unorganized radiative-convective equilibrium (RCE) over an ocean with uniform temperature. It is known, however, that in cloud-resolving model (CRM) studies of RCE, convection is preferentially triggered at cold-pool gust fronts, as demonstrated by Tompkins (2001, hereafter T01). Thus, a closer study of what happens at such gust fronts is necessary to understand how convection in RCE is generated.

That gust fronts in general can trigger convection (i.e., generate boundary layer plumes with significant vertical velocity) is well known, for example, from the study of squall lines (Weisman and Rotunno 2004) or mid-latitude continental convection (Droegemeier and Wilhelmson 1985). In these cases it has generally been assumed that the triggering is dynamical in nature—that is, that it arises from horizontal convergence at the gust front. For oceanic RCE, however, T01 noted that the thermal recovery of mature cold pools, along with

Corresponding author address: Nadir Jeevanjee, Department of Physics, University of California, Berkeley, 366 LeConte Hall MC 7300, Berkeley, CA 94720.
E-mail: jeevanje@berkeley.edu

pronounced moisture anomalies at the gust front, yield a dramatic reduction in convective inhibition (CIN) and enhancement of convective available potential energy (CAPE) there, pointing to a strong thermodynamic role for cold pools in organizing convection. While neither CIN nor CAPE directly relate to the generation of boundary layer mass flux, the thermal recovery of the mature cold pools pointed out by T01, along with the virtual effect due to the moisture anomalies at the gust front, raise the possibility that there is a significant buoyant contribution to the initial triggering. Our main goal in this paper is to assess this possibility, by evaluating the relative roles of mechanical and thermodynamical forces in generating mass flux at cold-pool gust fronts in oceanic RCE. We will focus on how low-level ($z = 300$ m) mass flux is generated and leave aside for the time being the question of how that low-level mass flux relates to cloud-base mass flux. Answering the latter question will be critical for solving the mass flux closure problem discussed above, and our work here can be seen as a first step in that direction.

Assessing the relative roles of thermodynamical and mechanical accelerations will require us to define these quantities, so we propose here the following simple definitions. We define the vertical buoyant acceleration [or “effective buoyancy”; Davies-Jones (2003, hereafter DJ03)] a_b to be the Lagrangian acceleration that would result if the wind fields were instantaneously zeroed out; that is,

$$a_b \equiv \left. \frac{dw}{dt} \right|_{\mathbf{u}=0}, \quad (1)$$

where $\mathbf{u} = (u, v, w)$ is the wind field. Up to a factor of $\bar{\rho}(z)$ (a reference density profile), this will be our “thermodynamic force.” We analogously define the vertical inertial acceleration a_i to be the Lagrangian vertical acceleration resulting from an instantaneous zeroing out of any horizontal density anomalies; that is,

$$a_i \equiv \left. \frac{dw}{dt} \right|_{\rho=\bar{\rho}}, \quad (2)$$

where ρ is the system density (including the weight of hydrometeors). Up to a factor of $\bar{\rho}$, this will be our “mechanical” or “dynamical” force, though it is really due entirely to inertia, as we will see.

We will show in the next section that $dw/dt = a_b + a_i$ and that a_b and a_i depend entirely on density and wind fields, respectively, and thus constitute a suitable decomposition of vertical force into thermodynamic and mechanical components. Mathematically equivalent decompositions are somewhat well known and have

been considered by previous authors (e.g., DJ03; Xu and Randall 2001; Krueger et al. 1995b), but the definitions (1) and (2) are new. In addition to bearing a simple physical interpretation, these definitions also yield unambiguous boundary conditions for a_b and a_i , which are often imposed by hand (DJ03; Klemp and Rotunno 1983) and can be a source of ambiguity (Markowski and Richardson 2011, p. 29).

A central feature of the definition (1) is that a_b includes both the Archimedean buoyancy B as well as the environmental response to the accelerations produced by B . We will see that a_b can be very different in magnitude and spatial distribution than B , to the degree that B cannot always be considered a first approximation for a_b . Thus, a proper determination of the character of convective triggering by cold pools depends crucially on considering a_b rather than B , as advocated by Doswell and Markowski (2004).

We begin by using the definitions (1) and (2) to derive diagnostic Poisson equations for a_b and a_i . With a proper force decomposition in hand, we then run a CRM in RCE and diagnose a_b and a_i at cold-pool gust fronts and across the entire domain. From this, we derive evidence that a_i is the primary driver behind tropical convective triggering and give a simple argument for why this should be. Our argument suggests that in the absence of cold pools, a_b may dominate; we confirm this by running a shallow-to-deep convection simulation, during which the dominant forcing transitions from a_b to a_i as precipitation sets in and cold pools appear.

2. Buoyant and inertial accelerations

a. Vertical force decomposition

We begin by deriving diagnostic equations for a_b and a_i . Our starting point is the anelastic momentum equation

$$\bar{\rho} \frac{d\mathbf{u}}{dt} = -\nabla p - \rho g \hat{\mathbf{z}}, \quad (3)$$

where p is the pressure and g is the gravitational acceleration. There is no Coriolis term as we are considering equatorial, oceanic RCE. A common approach is to approximate (3) by introducing a reference pressure profile $\bar{p}(z)$ in hydrostatic balance with $\bar{\rho}$, along with accompanying perturbations $p' \equiv p - \bar{p}$ and $\rho' \equiv \rho - \bar{\rho}$, which leads to

$$\frac{d\mathbf{u}}{dt} = B \hat{\mathbf{z}} - \frac{1}{\bar{\rho}} \nabla p', \quad (4)$$

where $B \equiv -\rho' g / \bar{\rho}$ is the usual Archimedean buoyancy. Here, however, we follow the approach taken in DJ03

and Das (1979) and alternatively decompose the pressure field as

$$p = p_h + p_{\text{nh}}, \quad (5a)$$

where

$$p_h \equiv \int_z^\infty dz' \rho g, \quad (5b)$$

so that p_h is the *local* hydrostatic pressure field and p_{nh} is the local nonhydrostatic pressure field. Plugging this into (3) yields

$$\bar{\rho} \frac{d\mathbf{u}}{dt} = -\nabla p_{\text{nh}} - \nabla_h p_h, \quad (6)$$

where $\nabla_h = \partial_x \hat{\mathbf{x}} + \partial_y \hat{\mathbf{y}}$ and we have an exact cancellation between the gravitational force and $-\partial_z p_h$. The z component of (6) is simply

$$\bar{\rho} \frac{dw}{dt} = -\partial_z p_{\text{nh}}, \quad (7)$$

so the Lagrangian vertical acceleration is given by $1/\bar{\rho}$ times the nonhydrostatic vertical pressure gradient force $-\partial_z p_{\text{nh}}$. [This result also dates back to List and Lozowski (1970) and Das (1979).] To apply the definitions (1) and (2), we must diagnose $\partial_z p_{\text{nh}}$. This can be achieved by taking the divergence of both sides of (6) and invoking anelastic mass continuity, which yields the Poisson equation

$$-\nabla^2 p_{\text{nh}} = \nabla \cdot [\bar{\rho}(\mathbf{u} \cdot \nabla)\mathbf{u}] + \nabla_h^2 p_h, \quad (8)$$

where ∇^2 is the usual three-dimensional Laplacian and $\nabla_h^2 \equiv \partial_x^2 + \partial_y^2$. Here, as in subsequent equations, we write the Laplacian term with a minus sign so that positive values on the right-hand side of the Poisson equation tend to generate positive responses in the solution (in this case, the solution for p_{nh}). Applying $-\partial_z$ to (8) yields

$$-\nabla^2(-\partial_z p_{\text{nh}}) = -\partial_z \nabla \cdot [\bar{\rho}(\mathbf{u} \cdot \nabla)\mathbf{u}] + g \nabla_h^2 \rho, \quad (9)$$

where we used the definition (5b) of p_h .

We can now combine the diagnostic equation in (9) with the result in (7) and the definition in (1) to obtain a Poisson equation for a_b :

$$-\nabla^2(\bar{\rho} a_b) = g \nabla_h^2 \rho. \quad (10)$$

Some remarks on this equation are in order. Note that it is horizontal density variations, as opposed to more general thermodynamic variations, that give rise to a_b , which is why we refer to it as a “buoyant” acceleration rather than a more general “thermodynamic” acceleration.

Also, up to the factor of $\bar{\rho}$, which makes our a_b an acceleration rather than a force per volume, (10) is identical to (6) of DJ03, so we adopt his nomenclature and alternatively refer to a_b as the “effective buoyancy.” Finally, an alternative diagnostic expression for the effective buoyancy can be obtained via (4); this is the approach used by most other authors (e.g., Doswell and Markowski 2004; Xu and Randall 2001; Krueger et al. 1995b), and we will compare and contrast these approaches in appendix A.

Next, we turn to the diagnosis of a_i . Combining (9), (7), and (2) yields the desired expression:

$$-\nabla^2(\bar{\rho} a_i) = -\partial_z \nabla \cdot [\bar{\rho}(\mathbf{u} \cdot \nabla)\mathbf{u}]. \quad (11)$$

Note that a_i is sourced by the advection of momentum, which is nothing but inertia, which is why we refer to a_i as an “inertial” acceleration. This quantity has appeared in the literature many times before, most often as the z component of a “dynamic” pressure gradient (e.g., Markowski and Richardson 2011; Rotunno and Klemp 1985; Klemp and Rotunno 1983). It will be both computationally and conceptually expedient for us to also consider $\bar{\rho} a_i$ as the vertical component of a pressure gradient. We will refer to the corresponding pressure field as the “inertial pressure,” denoted p_i , and we give the details of its definition, interpretation, and computation in appendix B.

Note that the determination of a_b and a_i via the Poisson equations (10) and (11) is incomplete without boundary conditions (BCs). We will be considering an atmosphere with rigid bottom ($z = 0$) and top ($z = z_t$), so that $w = 0$ at $z = 0$ and $z = z_t$. Equation (7) then implies $-\partial_z p_{\text{nh}} = 0$ at heights 0 and z_t . These BCs are unchanged by setting $\mathbf{u} = 0$ or $\rho = \bar{\rho}$, and so the definitions (1) and (2) yield the Dirichlet BCs $a_b = a_i = 0$ at $z = 0$ and $z = z_t$.

Finally, we observe that by (9)–(11), $\bar{\rho} a_b + \bar{\rho} a_i$ obeys the same Poisson equation as $-\partial_z p_{\text{nh}}$. Furthermore, both quantities have the same BCs. This tells us that $\bar{\rho} a_b + \bar{\rho} a_i = -\partial_z p_{\text{nh}}$, and (7) then implies

$$\frac{dw}{dt} = a_b + a_i. \quad (12)$$

Equation (12) is the desired decomposition of the vertical acceleration into buoyant and inertial components. Mathematically equivalent forms of (12) can be found elsewhere in the literature [e.g., Markowski and Richardson 2011, their (10.15); Krueger et al. 1995b; Xu and Randall 2001], and the derivation given here closely follows that given in DJ03 in many respects. The novel elements are the definitions (1) and (2), which yield unambiguous boundary conditions for a_b and a_i and give them a simple physical interpretation.

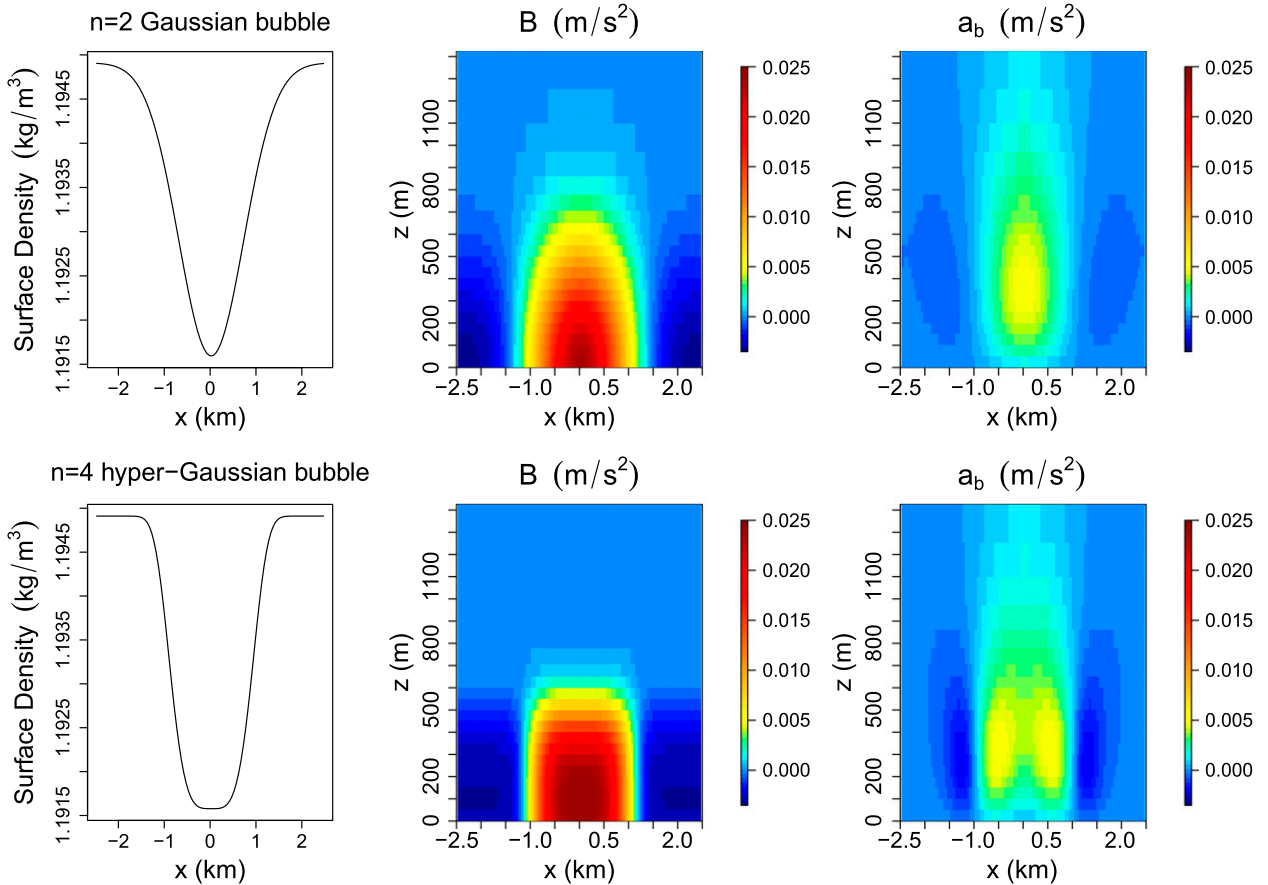


FIG. 1. An x - z cross section of (center) B and (right) a_b for Gaussian ($n = 2$) and hyper-Gaussian ($n = 4$) density perturbations of the form $\exp[-(r/r_0)^n - (z/z_0)^n]$. (left) The shape of the density perturbations at the surface is shown, and the precise form is given in the text. Note that a_b is only a fraction of B throughout most of both bubbles and that a_b is nonzero above $z \sim 1000$ m, where $B \approx 0$. Also note the double peak in a_b for the broad $n = 4$ distribution.

b. Contrasting Archimedean and effective buoyancies

Before describing our experiments and their results, let us get a feel for how a_b works and how it differs from Archimedean buoyancy (some intuition for a_i and p_i is developed in appendix B). From (10), we see that a_b is sourced by the horizontal Laplacian of ρ , so that buoyant accelerations tend to be strongest at local extrema of density (or, more generally, regions of $g\nabla_h^2\rho \neq 0$) rather than at density anomalies defined relative to an arbitrary reference value (as with B). This means that a_b of a parcel is defined relative to its immediate surroundings, so that a very warm parcel surrounded by other warm air may accelerate less than a moderately warm parcel surrounded by cool air.

Since (10) is a Poisson equation, effective buoyancy is nonlocal: that is, localized extrema of density give rise to accelerations everywhere, even where $B = 0$. This is, of course, because any localized acceleration must (by

mass continuity) be accompanied by compensating accelerations in the rest of the atmosphere. These compensating accelerations (see appendix A for their definition) often oppose the buoyancy field that gives rise to them (Markowski and Richardson 2011; Houze 1994), yielding a reduced net acceleration for air with significant B . For isolated regions of significant buoyancy, we thus expect that $|a_b| < |B|$.

These aspects of a_b are illustrated in Fig. 1, which shows x - z cross sections of B and a_b for two Gaussian bubbles of the form

$$\rho = \bar{\rho}(z) + \delta\rho \exp[-(r/r_0)^n - (z/z_0)^n]$$

for $n = 2$ and 4. Here, $r_0 = 1$ km, $z_0 = 500$ m, and $\delta\rho = \bar{\rho}(0)/300$, where $\bar{\rho}(z)$ is taken from our RCE simulations described below. We calculate B with respect to the horizontal average of ρ rather than $\bar{\rho}$; the fact that such a choice is required, yet somewhat

arbitrary, is yet another shortcoming of B (Doswell and Markowski 2004).

Perhaps the most striking feature (for both values of n) of Fig. 1 is the degree to which $|a_b| < |B|$, requiring a rather severe stretching of the color bar to render features of both fields visible. Another interesting feature of Fig. 1, particularly for $n = 4$, is that for $z \gtrsim 1000$ m, $a_b \neq 0$ even though $B \approx 0$. As discussed above, this is because a_b not only accelerates the bubble but also sets up the accompanying environmental circulation.

Finally, for $n = 4$, one can calculate that $\nabla_h^2 \rho$ is a maximum near the “shoulder” of the density distribution at $r \approx 500$ m, and Fig. 1 shows a corresponding maximum there in the a_b field as well. This is to be contrasted with the B field, where the maximum is found at $r = 0$, where ρ itself has a minimum. Again, this is because net thermodynamic accelerations are a function of how buoyant a parcel is relative to its immediate surroundings, and so when the peak of the density distribution is too broad, the parcels there feel less acceleration than their counterparts at the shoulder of the distribution. Thus, the spatial distribution of a_b can indeed differ from that of B ; we will see even more dramatic examples of this in the next section.

3. RCE simulations

With a preliminary understanding of a_b in hand, we can proceed to investigate whether a_b or a_i dominates the triggering of deep convection by cold pools in CRM simulations of RCE. This section describes the numerical model used as well as our specific case setup. We also briefly describe our calculation of a_b and a_i ; this is discussed in greater detail in appendix B.

Our cloud-resolving simulations were performed with Das Atmosphärische Modell (DAM) (Romps 2008). DAM is a three-dimensional (3D), fully compressible, nonhydrostatic CRM, which employs the six-class Lin–Lord–Krueger microphysics scheme (Lin et al. 1983; Lord et al. 1984; Krueger et al. 1995a). Radiation is interactive and is calculated using the Rapid Radiative Transfer Model (Mlawer et al. 1997). We rely on implicit LES (Margolin et al. 2006) for subgrid-scale transport, and thus no explicit subgrid-scale turbulence scheme is used.

Our RCE simulations ran on a square doubly periodic domain of horizontal dimension $L = 51.2$ km, with a horizontal resolution of $dx = 100$ m. The vertical grid stretches smoothly from 50-m resolution below 1200- to 100-m resolution above, up to the model top at 30 km. We ran with a fixed sea surface temperature of 300 K and calculated surface heat and moisture fluxes using a bulk aerodynamic formula.

For a first diagnosis of a_b and a_i in RCE, we spun up the model for 60 days on an $L = 12$ -km, $dx = 200$ -m domain, then used the vertical profiles from this run to initialize a 13-day run on an $L = 51$ -km, $dx = 200$ -m domain. This run was then restarted with $dx = 100$ m and run for one more day to iron out any artifacts from changing the resolution. All data in the next section are from the end of this run.

We diagnose a_b directly from CRM output via the Poisson equation (10). We compute a_i slightly indirectly by first computing the inertial pressure p_i from CRM output via (B2) and then using $a_i = -(\partial_z p_i)/\bar{\rho}$. We solve both Poisson equations by Fourier transforming in the horizontal, which yields systems of algebraic equations that can be solved by inverting a tridiagonal matrix. As discussed in section 2a, the fact that $w \equiv 0$ at model top and bottom yields Dirichlet boundary conditions for a_b and Neumann boundary conditions for p_i . The implementation of the latter is somewhat subtle, however, and requires some care; see appendix B for details.

4. RCE results

Plan views of the vertical velocity w at $z = 300$ m as well as the vertical accelerations B , a_i , and a_b at $z = 150$ m for a CRM snapshot are given in Fig. 2. Cold pools are clearly visible in the B field, and incipient convection at the cold-pool gust fronts is evident in the w field. Comparison of a_i and a_b suggests that this incipient convection is due primarily to a_i rather than a_b . Note the much reduced magnitude and differing spatial scales of a_b relative to B , again requiring a severely stretched color bar; in this circumstance, B is not even a first approximation for a_b . This drastic difference between a_b and B is a result of the extreme aspect ratio of the cold pools as well as their proximity to the ground, where an $a_b = 0$ boundary condition is enforced. Further work is needed to separately quantify these two effects and delineate the density distribution regimes over which B can be used as a proxy for a_b .

To further investigate the dominance of a_i over a_b , we take an y - z transect through a particular cold-pool gust front from Fig. 2 and plot various quantities for this transect in Fig. 3. (This particular gust front is marked with a black circle in the w plot of Fig. 2.) We see a vigorous southward-moving cold pool with a gust front at $y \approx 38$ km as well as a nascent plume ($w > 1$ m s⁻¹) just above at around $z = 300$ m. The warm, moist air feeding this plume from below is visible in the B , θ , q_v , and θ_e fields at $(y, z) \approx (38 \text{ km}, 150 \text{ m})$, and the gust front and plume indeed exhibit anomalously high θ_e , as noted by T01. Despite such thermodynamic enhancement, however, the plume’s near-surface acceleration is strongly

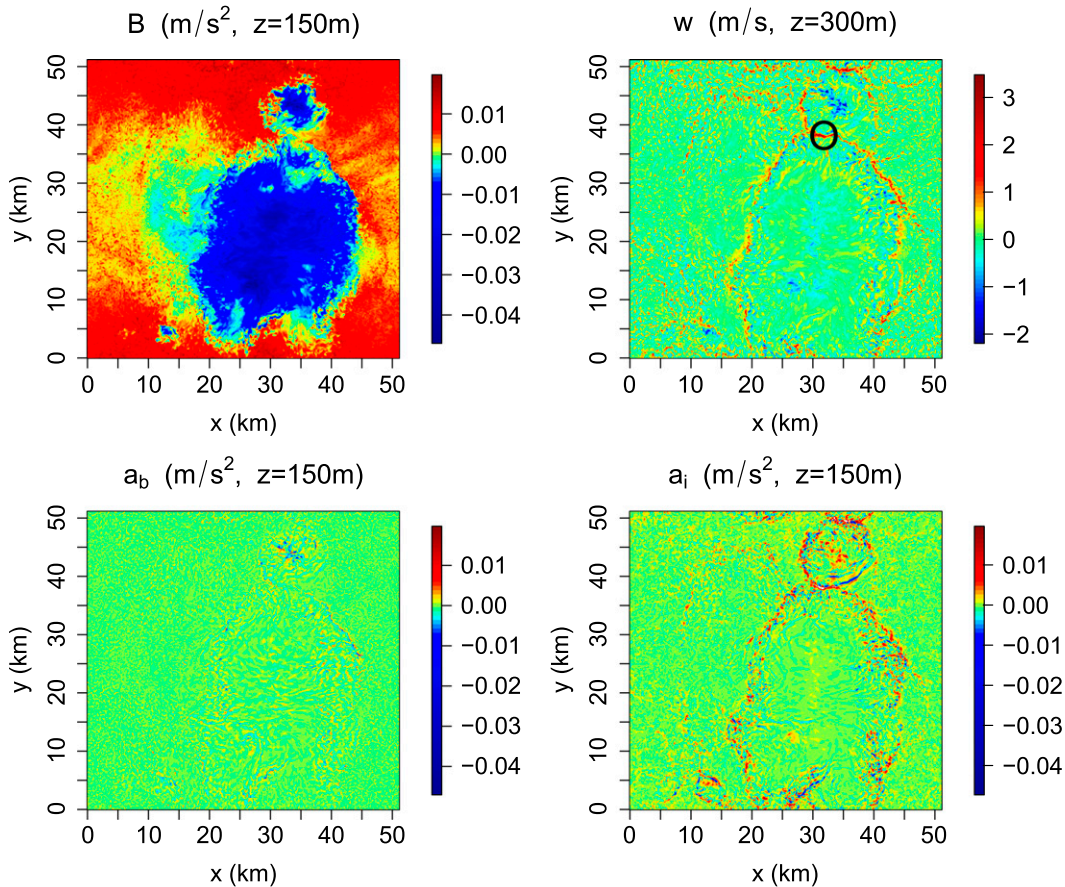


FIG. 2. Plot of B , w , a_b , and a_i in the boundary layer for a CRM snapshot. Note that incipient convection ($w \geq 1 \text{ m s}^{-1}$) is almost entirely collocated with the cold-pool boundaries visible in the B field and that the vertical acceleration there appears strongly dominated by a_i . Note the stretched color bar for all accelerations. The black circle in the w plot marks the gust front whose transect is plotted in Fig. 3.

dominated by a_i . Even when plotted on a stretched color scale, its a_b is barely discernible and is much reduced relative to its Archimedean buoyancy, consistent with our results from section 2b.

To quantitatively test the hypothesis that the a_i spike is responsible for the nascent plume, we check if w of the nascent plume at $z = 300 \text{ m}$, which is about 2.5 m s^{-1} , is equal to $\sqrt{2a_i h}$ where h is the height of the a_i spike at the gust front. Taking $a_i \approx 0.02 \text{ m s}^{-2}$ and $h \approx 200 \text{ m}$ gives $\sqrt{2a_i h} = 2.8 \text{ m s}^{-1}$, which is consistent with the actual w .

We analyzed several other cold pools and came to similar conclusions. Still, a more comprehensive and objective test of the dominance of a_i is needed. To that end, we identify “active” columns [defined here to be those (x, y) with $w(x, y, z = 300 \text{ m}) > 0.5 \text{ m s}^{-1}$], and for these regress $\bar{p}a_i$ and $\bar{p}a_b$ evaluated at $(x + \delta x, y + \delta y, z)$, for various $\delta x, \delta y$, and z , against $w^2(x, y, 300 \text{ m})$. This yields regression coefficients $r_b(\delta x, \delta y, z)$ and $r_i(\delta x, \delta y, z)$ which are least squares fits to

$$\begin{aligned} a_b(x + \delta x, y + \delta y, z) &= r_b(\delta x, \delta y, z) \cdot w^2(x, y, 300 \text{ m}) + C_b, \\ a_i(x + \delta x, y + \delta y, z) &= r_i(\delta x, \delta y, z) \cdot w^2(x, y, 300 \text{ m}) + C_i, \end{aligned} \quad (13)$$

where the intercepts C_b and C_i are negligible and ignored henceforth. We use w^2 rather than w because (by the work-energy theorem) a linear relationship with the forces is expected only for w^2 . We regress the forces on w^2 , rather than the other way around, because we want the regression coefficient to be directly proportional, rather than inversely proportional, to the magnitude of the forces. Maps of r_b and r_i as a function of $(\delta x, \delta y)$ and at various heights z are shown in Fig. 4. [The units and order of magnitude of the coefficients are given by $\rho/2h = (1.2 \text{ kg m}^{-3})/(2 \times 200 \text{ m}) = 0.003 \text{ kg m}^{-4}$.] These maps show clearly and objectively the dominance of a_i over a_b in generating new mass flux in the boundary layer and constitute our main numerical result.

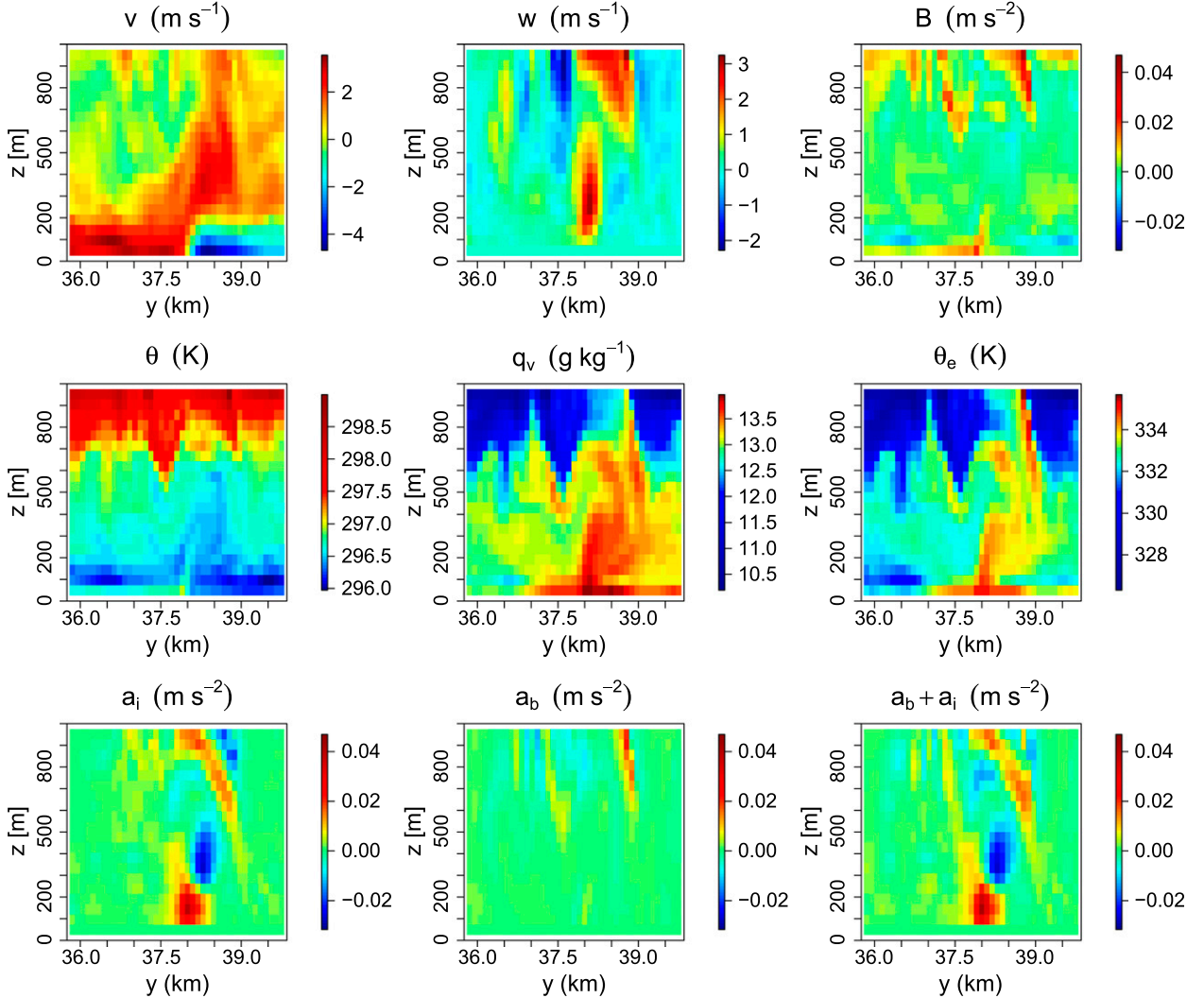


FIG. 3. Plot of v , w , B , θ , q_v , θ_e , a_i , a_b , and $a_b + a_i$ for cold-pool transect. The nascent plume at $(x, y) = (38 \text{ km}, 150 \text{ m})$, visible in the w field, lies just above the gust front evident in the u field. The plume has anomalously high θ , q_v , and B but is nonetheless triggered primarily by a_i . Note again the drastic differences in the a_b and B fields.

5. Why does a_i dominate?

The previous section presented anecdotal as well as systematic evidence that a_i dominates over a_b in triggering new low-level mass flux in a simulation of deeply convecting RCE. It remains, however, to gain some insight as to why this should be. In this section we will estimate the ratio of a_i to a_b at a cold-pool gust front by estimating the ratio of the relevant source terms in their respective Poisson equations. We justify this approach by noting that variations in a_b and a_i at the gust front occur over the same length scales and so $\nabla^2 a_i / \nabla^2 a_b \approx a_i / a_b$.

First consider the source term $S_{a_i} \equiv -\partial_z \nabla \cdot [\bar{\rho}(\mathbf{u} \cdot \nabla) \mathbf{u}]$ for a_i in (11). This can be rewritten as

$$S_{a_i} = \partial_z [\bar{\rho}(\partial_j u_i)(\partial_i u_j) - \bar{\rho} w^2 \partial_z^2 \ln \bar{\rho}]. \quad (14)$$

To analyze this, note that the scale of $\bar{\rho}$ variations is much larger than those for the velocities, so we can neglect derivatives of $\bar{\rho}$. This leaves us with

$$S_{a_i} = \bar{\rho} \partial_z [(\partial_j u_i)(\partial_i u_j)]. \quad (15)$$

Let us evaluate this at a gust-front boundary, where U is a typical horizontal velocity of the front, W is a typical vertical velocity of a triggered updraft, h is a typical height of the front, and L is the length over which u and B transition from their cold-pool values to their ambient values. (From the surface level in Fig. 3,

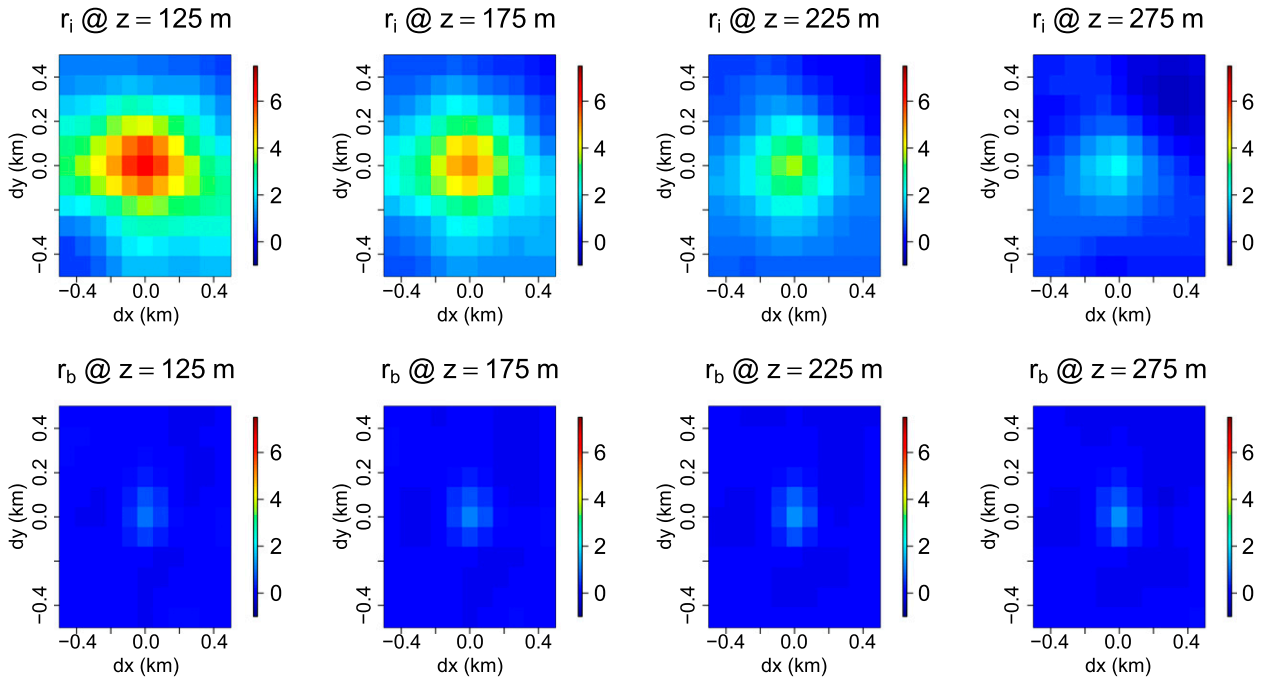


FIG. 4. Regression coefficients r_i and r_b (g m^{-4}) as defined in (13), plotted as a function of δx and δy , respectively, for various z . This more objective and comprehensive test again shows that a_i dominates over a_b .

this is evidently the grid spacing dx , though we will see that our argument is resolution independent.) Then every $i = 1$ or 2 in (15) yields a factor of U/L , and every factor of $i = 3$ yields a factor of W/h , which equals U/L by continuity. The same is true for j . Also, ∂_z contributes a factor of $1/h$, and so we can estimate (15) as

$$S_{a_i} \approx 9\bar{\rho} \frac{U^2}{L^2 h}.$$

Similarly, the source term for a_b is given by

$$S_{a_b} \equiv g \nabla_h^2 \rho' \approx 2g \frac{\rho'}{L^2},$$

where ρ' is a characteristic density anomaly for a cold pool. Taking the ratio of our expressions for S_{a_i} and S_{a_b} gives

$$\frac{S_{a_i}}{S_{a_b}} \approx \frac{9U^2}{2Bh}, \quad (16)$$

where B is a characteristic magnitude of Archimedean buoyancy for the cold pool. To evaluate (16), we use the empirical observation (Hacker et al. 1996) that for a lock-release density current, the ‘‘total depth’’ Froude number ($\text{Fr}_H \equiv U/\sqrt{B_0 H}$) is roughly equal to $1/2$,

independent of time and H .¹ Here H is a characteristic height for the negatively buoyant downdraft that spawned the cold pool, and B_0 is the magnitude of the cold pool’s initial buoyancy (typically $B_0 \gtrsim B$). Plugging $U^2 = 0.5B_0 H$ into (16) gives

$$\frac{S_{a_i}}{S_{a_b}} \approx \frac{9}{4} \frac{B_0 H}{Bh} > 1. \quad (17)$$

This is our main theoretical result. Taking typical values of $H = 800$ m, $h = 200$ m, $B_0 = 0.02 \text{ m s}^{-2}$, and $B = 0.01 \text{ m s}^{-2}$ gives a ratio of about 18, implying that, at the gust fronts, a_i is larger than a_b by about an order of magnitude. This corresponds roughly to what we see in Figs. 2 and 3. A cartoon of this result, emphasizing the ratio of H to h as a determining factor in the dominance of a_i over a_b , is given in Fig. 5.

6. Shallow-to-deep simulation

Given that we have identified a_i as the dominant force component in the generation of boundary layer mass

¹ More specifically, if the initial slug has a radius R_0 , then Fr_H is roughly constant until the gust front reaches $8\text{--}10R_0$, at which point the cold pools in our simulation have transitioned to warm pools.

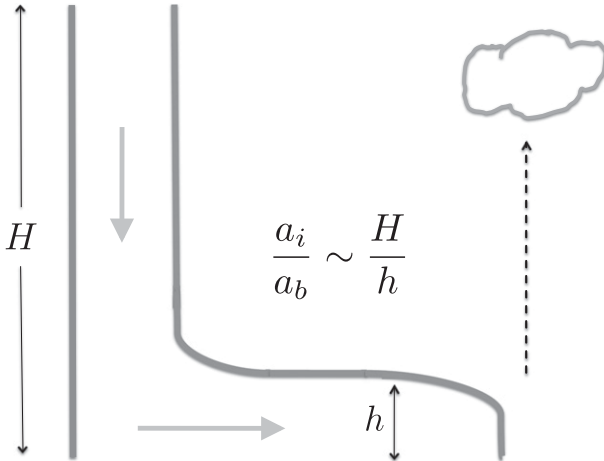


FIG. 5. Cartoon depicting the dominance of a_i over a_b as resulting primarily from the ratio of H to h , as in (17).

flux in RCE, it is of interest to ask whether there are other settings in which a_b , rather than a_i , might dominate. One might expect that for shallow nonprecipitating convection, the absence of cold pools would mean that the triggering of convection is primarily buoyant in nature.

To test this, we run a shallow-to-deep CRM simulation similar to that of [Kuang and Bretherton \(2006\)](#), where we use the same model domain and grid spacing as for our RCE simulation above but initialize with a thermodynamic profile based on observations from the Barbados Oceanography and Meteorology Experiment (BOMEX). For heights between 0 and 3000 m we use the θ and q_v profiles given in the CRM intercomparison study of this case in [Siebesma et al. \(2003\)](#). We then simply (and somewhat crudely) extend the θ profile above 3000 m by linearly interpolating (z, θ) to a tropopause at (14 000 m, 350 K) and then to the model top at (30 000 m, 800 K). We similarly extend the q_v profile via relative humidity (RH) by interpolating (z, RH) to (14 000 m, 0.5) and then to (30 000 m, 0). These values roughly approximate those found in our RCE simulations. We fix the latent heat flux at 150 W m^{-2} and sensible heat flux at 10 W m^{-2} , in accordance with [Siebesma et al. \(2003\)](#). Note the contrast with other studies of the shallow-to-deep transition, such as [Kuang and Bretherton \(2006\)](#) and [Böing et al. \(2012\)](#), where the transition is forced by time-dependent surface fluxes. Here, we are less interested in a realistic transition between shallow and deep convection as we are in contrasting their convective triggering mechanisms, and we deem this simple simulation sufficient for that purpose.

We run this simulation for 2 days, saving 3-hourly snapshots. For each snapshot, we calculate r_b and r_i as in (13) but set $\delta x = \delta y = 0$ for clarity. We thus get one value

of r_b and r_i at each height for each snapshot, and time series of these (along with domain-mean precipitation) are presented in [Fig. 6](#). Indeed, we see that a_b dominates while precipitation is negligible and that a_i takes over as precipitation sets in; this confirms our expectation and provides a clear hydrodynamical distinction between mass flux generation in the two regimes.

7. Implications

We have used a carefully chosen formulation of the anelastic equations of motion to decompose vertical accelerations into inertial and buoyant components and have used the resulting decomposition to analyze the triggering of low-level mass flux by cold-pool gust fronts. This can be seen as a first step toward answering the question of how cloud-base mass flux is generated in the boundary layer of an atmosphere in deeply convecting RCE. Along the way, we have also developed some intuition for the inertial and buoyant accelerations and have addressed some ancillary questions that arise in their interpretation and computation.

The notion of effective buoyancy, though not new, has received relatively little attention. The physics that it embodies is well known, in that it is widely acknowledged in the literature that buoyant accelerations of parcels are reduced by back reaction from the environment and that this effect depends on the horizontal extent of the parcel, but these effects are rarely computed explicitly. Furthermore, widely used diagnostic quantities such as CAPE and CIN, which play central roles in various convective parameterizations (e.g., [Zhang and McFarlane 1995](#); [Bretherton et al. 2004](#)), are based on easily calculated Archimedeian buoyancy, rather than on the complete buoyant force.² Since the results presented here (and in particular [Figs. 1](#) and [2](#)) suggest that Archimedeian buoyancy can be highly inadequate in capturing buoyant acceleration, both in magnitude and spatial distribution, care must be taken in the quantitative application of such diagnostics. If a parcel's CIN, for instance, is a poor estimate of the negative buoyant acceleration it experiences as it makes its way to cloud base, then there may be little theoretical justification for the CIN-TKE mass flux closures employed in, for example, [Mapes \(2000\)](#) and [Bretherton et al. \(2004\)](#). There is thus a need for a simple yet quantitatively reliable way to estimate the effective buoyancy of a parcel given some additional datum about its spatial dimensions and proximity to the ground.

² As computed via a_b , or by adding in the buoyancy perturbation pressure force $-\partial_z p'_b$, as per (A1) below.

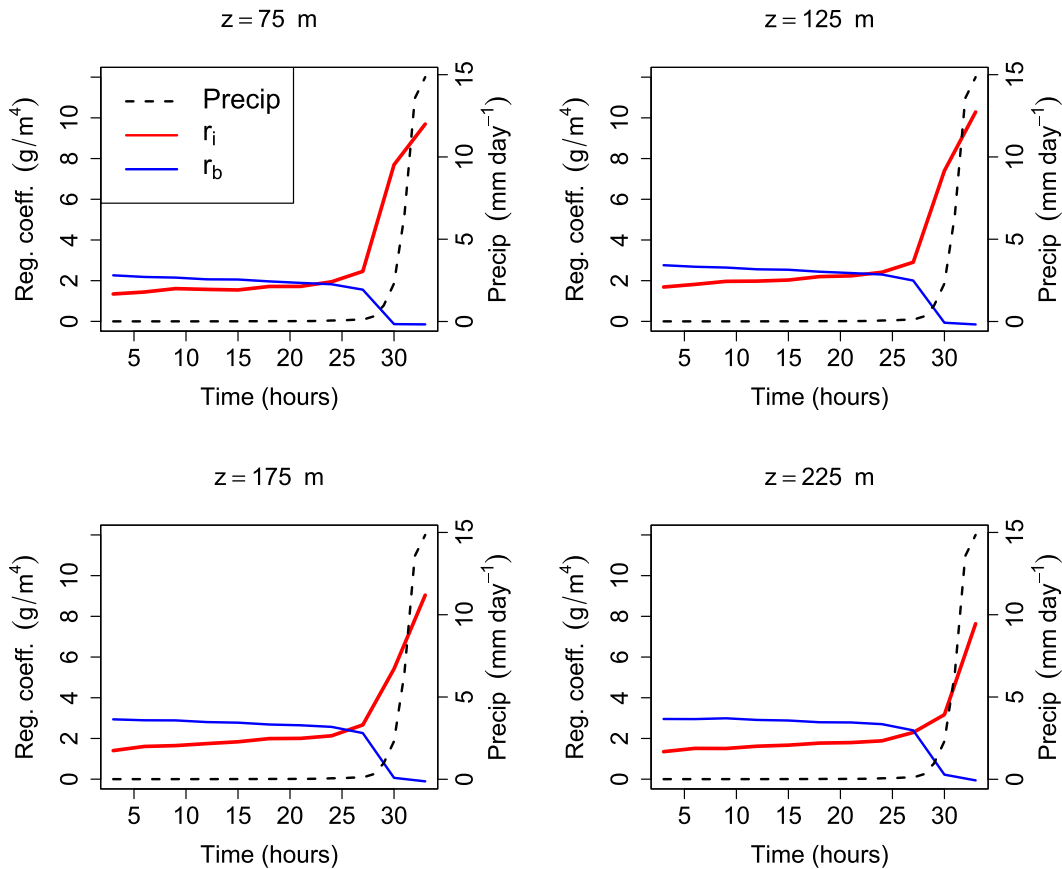


FIG. 6. Time series of r_i and r_b , computed as in (13) for various z but with $\delta x = \delta y = 0$, along with precipitation time series, for the shallow-to-deep simulation. Note that a_b dominates before precipitation sets in, at which point a_i takes over.

The other component of vertical force, the inertial pressure gradient ($\bar{p}a_i = -\partial_z p_i$), seems to be more familiar than effective buoyancy, having in particular played a key role in the analysis of severe storms and tornadoes (e.g., Rotunno and Klemp 1985; Klemp and Rotunno 1983; Markowski and Richardson 2011). Despite this exposure though, p_i remains slightly enigmatic. There seems to be little discussion in the literature of p_i as an enforcer of mass continuity in the face of inertial motions and how this implies that strain and vorticity generate p_i disturbances of opposing sign. Furthermore, the calculation of p_i via (B2) raises issues of boundary-condition implementation and finite-difference interpolation that often go unmentioned but actually require rather exquisite care. We have endeavored to fill these gaps in the interpretation and calculation of p_i in appendix B.

Finally, our result that the inertial acceleration a_i dominates the low-level triggering of new mass flux provides a stepping stone to a more complete picture of mass flux generation in the boundary layer. Though we

have not made a precise connection between the low-level mass flux investigated here and cloud-base mass flux, a positive correlation is to be expected, and thus our results lend preliminary support to convective parameterizations in which the inertial triggering of mass flux at cold-pool gust fronts takes center stage, as in Rio et al. (2013).

Of course, many details remain to be filled in. For instance, the origins of the anomalous moisture at the gust front remain uncertain. Surface fluxes and entrainment of environmental air are potential sources of both heat and moisture for the gust front, which may have already been significantly premoistened by evaporating precipitation, but a quantification of these various sources is still lacking. Also, although a_i dominates over a_b in the lower boundary layer, the transect in Fig. 3 (as well as other transects that we inspected) suggest that the force balance may shift as the plume rises and that a_b may play a role in shepherding nascent plumes through the middle boundary layer and up to their lifting condensation levels. Quantifying this role would be

necessary to complete the picture of cloud-base mass flux generation.

Apart from the generation of deep convective mass flux, there are other problems that might be fruitfully analyzed with the approaches taken here. It could be helpful to attempt a scaling estimate for a_i/a_b as in (17), but for shallow convection, where turbulent motions instead of cold pools are responsible for generating the heterogeneity in density and wind that generate a_b and a_i . Also, applying the force decomposition in (12) to convection in the free troposphere could further refine our picture of the vertical momentum budget of thermals, as recently studied in, for example, Wang and Zhang (2014), Sherwood et al. (2013), and de Roode et al. (2012).

Finally, we note that as we were revising this paper, a similar study was published that also examines the relative influence of thermodynamic and mechanic properties of cold pools upon convective triggering (Torri et al. 2015). Similar to this study, those authors also found that mechanical forces dominate over thermodynamic ones in triggering low-level mass flux. Furthermore, they employed a Lagrangian particle dispersion, which allowed them to quantify the influence of cold-pool thermodynamics in reducing particles' lifting condensation levels. They also introduced a novel algorithm for tracking the lifetimes of cold pools and the residence times of particles within them, providing new insights into the origins of mass flux triggered by cold pools.

Acknowledgments. This work was supported by the U.S. Department of Energy's Earth System Modeling, an Office of Science, Office of Biological and Environmental Research program under Contract DE-AC02-05CH11231. This research used computing resources of the Extreme Science and Engineering Discovery Environment (XSEDE), which is supported by National Science Foundation Grant OCI-1053575. N.J. thanks Wolfgang Langhans for discussions and assistance.

APPENDIX A

Comparison of Two Approaches to Effective Buoyancy

Solving (10) is not the only way to obtain the buoyant acceleration. One can use the momentum equation [(4)] and take its divergence to obtain a Poisson equation for p' , which has $-\bar{\rho}\partial_z B$ as one of its source terms. One can then define a "buoyancy perturbation pressure" p'_b as the solution to $-\nabla^2 p'_b = -\bar{\rho}\partial_z B$ [modulo ambiguous

boundary conditions; Markowski and Richardson (2011, p. 29)], and it can be shown (DJ03) that

$$a_b = B - (\partial_z p'_b)/\bar{\rho}. \quad (\text{A1})$$

Thus, one can compute a_b by computing B , solving $-\nabla^2 p'_b = -\bar{\rho}\partial_z B$, and then summing. This approach has been taken by other authors (e.g., Xu and Randall 2001; Krueger et al. 1995a). Though the two approaches must yield the same result, they lend themselves to different interpretations. The $B - (\partial_z p'_b)/\bar{\rho}$ expression says that Archimedean buoyancy drives buoyant accelerations and $-(\partial_z p'_b)/\bar{\rho}$ gives the environmental response. To analogously interpret a_b as computed via (10), we proceed as follows. We define a "buoyancy pressure" p_b (not to be confused with the buoyancy perturbation pressure p'_b) as the p_{nh} field resulting from zeroing out the wind fields (i.e., $p_b \equiv p_{\text{nh}}|_{\mathbf{u}=0}$). It follows from (8) that

$$-\nabla^2 p_b = \nabla_h^2 p_h, \quad (\text{A2})$$

and so p_b arises to enforce mass continuity in the face of horizontal hydrostatic pressure forces $-\nabla_h p_h$. Furthermore, (19) implies $a_b = -\partial_z p_b/\rho$, and hence the buoyant acceleration a_b can be seen as the vertical acceleration needed to compensate for horizontal motions driven by the hydrostatic pressure gradient, as in the stack (or "chimney") effect.

We thus have two ways of thinking about the buoyant force. One significant disadvantage of the $B - (\partial_z p'_b)/\bar{\rho}$ approach is that it treats B as primary, even though B suffers significant arbitrariness because of its dependence on an arbitrary reference state [as pointed out in section 2b and emphasized by Doswell and Markowski (2004)]. The a_b approach does not suffer this ambiguity and also lends itself to a straightforward derivation of (17).

APPENDIX B

Defining, Interpreting, and Calculating the Inertial Pressure

a. Defining and interpreting p_i

We mentioned in section 2a that a_i can be viewed as the z component of the gradient of an associated pressure, the inertial pressure p_i , defined here as

$$p_i \equiv p_{\text{nh}}|_{\rho=\bar{\rho}}. \quad (\text{B1})$$

Applying this definition to (6) and taking its divergence yields the following Poisson equation for p_i :

$$-\nabla^2 p_i = \mathbf{V} \cdot [\bar{\rho}(\mathbf{u} \cdot \nabla)\mathbf{u}]. \quad (\text{B2})$$

Equation (7) yields Neumann boundary conditions (BCs) $\partial_z p_i = 0$ at model top and bottom. Applying $-\partial_z$ to both sides of this equation, comparing with (11), and noting that Neumann BCs for p_i imply Dirichlet BCs for $\partial_z p_i$ show that indeed $\bar{\rho} a_i = -\partial_z p_i$.

Equation (B2) can be interpreted as enforcing the cancellation of the tendency of mass divergence generated by the inertial pressure with that generated by advection, in order to maintain anelastic continuity. In other words, the p_i field produces whatever force is needed to ensure (anelastic) mass continuity in the face of the divergent tendencies generated by fluid inertia.

To gain further intuition for p_i , we refer to Bradshaw and Koh (1981), who showed that the source term S_{p_i} , which we define to be the right-hand side of (B2), can be written (neglecting $\bar{\rho}$ variations) as

$$S_{p_i} = \bar{\rho} \left(\|\mathbf{e}\|^2 - \frac{1}{2} \|\boldsymbol{\omega}\|^2 \right), \quad (\text{B3})$$

where \mathbf{e} is the strain tensor with components $e_{ij} = 1/2(\partial_i u_j + \partial_j u_i)$, $\boldsymbol{\omega}$ is the vorticity vector with components $\omega_i = \epsilon_{ijk} \partial_j u_k$, and the norm squared $\|\cdot\|^2$ of a vector or matrix denotes the sum of the squares of the components. Thus, strain is a source of positive pressure and vorticity a source of negative pressure.

We can understand this as follows. First consider a 2D velocity field \mathbf{u} , vanishing at infinity, that, to first order around the origin, is given by the solid-body rotation field $\mathbf{u} = (-y, x)$ (Fig. B1a). If \mathbf{u} is allowed to evolve solely under its own inertia, then, near the origin,

$$\partial_t \mathbf{u} = -(\mathbf{u} \cdot \nabla)\mathbf{u} = (x, y).$$

In other words, \mathbf{u} will develop a component pointing radially outward from the origin (Fig. B1b) as a consequence of the familiar centrifugal “force.” This advective tendency will cause a divergence of mass, and since it is the job of p_i to generate a convergence of mass to counteract this, p_i must have a low at the origin. Thus, vorticity must be a source of negative p_i .

Next, consider another \mathbf{u} field that vanishes at infinity but is given to first order at the origin by the irrotational field $\mathbf{u} = (-x, y)$ (Fig. B1c). This field converges along the x axis and diverges along the y axis and thus has nonzero strain at the origin. If \mathbf{u} is allowed to evolve solely under its own inertia, then, near the origin,

$$\partial_t \mathbf{u} = -(\mathbf{u} \cdot \nabla)\mathbf{u} = (-x, -y).$$

In other words, \mathbf{u} will develop a component pointing radially inward toward the origin (Fig. B1d). This

advective tendency will cause a convergence of mass, and since it is the job of p_i to generate a divergence of mass to counteract this, p_i must have a high at the origin. Thus, strain must be a source of positive p_i .

b. Calculating p_i

When calculating p_i , it is computationally expedient to rewrite S_{p_i} yet again to obtain the Poisson equation

$$-\nabla^2 p_i = \bar{\rho}(\partial_j u_i)(\partial_i u_j) - w^2 \partial_z^2 \ln \bar{\rho}. \quad (\text{B4})$$

[The z derivative of this is just the right-hand side of (14).] We solve (B4) by first Fourier transforming from (x, y) to $\mathbf{k} = (k_x, k_y)$ in the horizontal, periodic dimensions, which yields a set of algebraic equations for each \mathbf{k} which are coupled only in z . This system can be written in terms of a \mathbf{k} -dependent tridiagonal matrix, which is (in general) easily inverted, whereupon we Fourier transform back and are done.

One issue that deserves further comment is that of the boundary conditions at model top ($z = z_t$) and model bottom ($z = 0$). As noted above, p_i obeys the Neumann BCs

$$\partial_z p_i(z_t) = \partial_z p_i(0) = 0. \quad (\text{B5})$$

The rub is that these double Neumann BCs do not uniquely specify p_i but only determine it up to a constant; thus, these BCs are degenerate. This manifests computationally in a noninvertible tridiagonal matrix for $\mathbf{k} = 0$ —that is, the constant Fourier component $\bar{p}_i(z)$ (denoting horizontal averages with an overbar). We can thus keep our Neumann BCs for $\mathbf{k} \neq 0$ as well as for \bar{p}_i at model bottom and then specify our constant and remove the degeneracy by imposing the Dirichlet BC $\bar{p}_i(z_t) = 0$ at model top. This, however, seems potentially inconsistent with (B5), which implies $\partial_z \bar{p}_i(z_t) = 0$ as well. Fortunately, the Poisson equation carries an integral constraint that saves the day. Integrating (B2) over the entire domain, noting that the boundary of the domain consists of just the model top and bottom, and applying the divergence theorem yields

$$-\iint dx dy \partial_z p_i|_0^{z_t} = \iint dx dy \bar{\rho}(\mathbf{u} \cdot \nabla)w|_0^{z_t}. \quad (\text{B6})$$

The fact that $w \equiv 0$ at $z = 0$ and $z = z_t$ implies that the right-hand side of (B6) is zero. At the same time, one can recognize the left-hand side as $\partial_z \bar{p}_i(z_b) - \partial_z \bar{p}_i(z_t)$ times a constant. This yields the constraint

$$\partial_z \bar{p}_i(0) = \partial_z \bar{p}_i(z_t). \quad (\text{B7})$$

Thus, the Neumann BC at model bottom plus the constraint (B6) implies that the Neumann BC holds

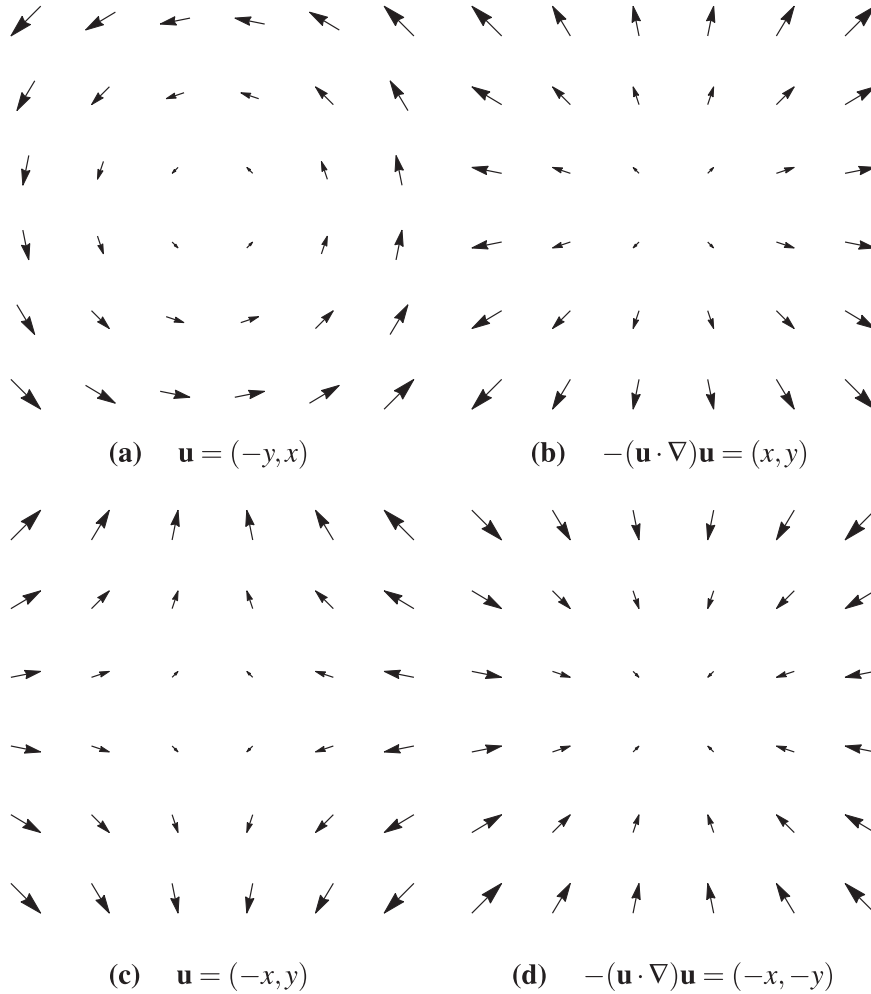


FIG. B1. Idealized vector fields and their advective tendencies. (a) A pure rotational flow and (b) its divergent advective tendency. (c) A pure (irrotational) strain flow and (d) its convergent advective tendency. The inertial pressure balances these tendencies by generating a low (high) at the origin in the case of pure rotation (strain).

at model top as well, in addition to our Dirichlet BC there.

As an aside, we should note here that numerically, the summed source term $\bar{p}(\partial_j u_i)(\partial_i u_j)$ on the right-hand side of (B4) must be quite carefully computed in order for the constraint (B7) to be obeyed. In particular, on an Arakawa C grid (Arakawa and Lamb 1977) the terms with different (i, j) live at different points of the grid cell, but for a given (i, j) each factor $\partial_j u_i$ and $\partial_i u_j$ lives on the same point of the grid cell. To compute S_{p_i} , one must interpolate each term to a common point before summing, but it is imperative to only perform this interpolation after multiplying $\partial_j u_i$ and $\partial_i u_j$ together. We found that interpolating before multiplying yielded a p_i field that did not obey (B7).

Returning to analytics, we observe that one can, in fact, go beyond the constraint in (B7) and obtain an explicit expression for \bar{p}_i . We begin with the anelastic equation of motion

$$\bar{p} \frac{dw}{dt} = \bar{p} a_b - \partial_z p_i \tag{B8}$$

and take a horizontal average over our domain with area A . We evaluate $\bar{p} \bar{a}_b$ by applying a horizontal average to (10), which yields $-\partial_z^2(\bar{p} \bar{a}_b) = g \nabla_h^2 \bar{\rho} = 0$. This, along with the BCs $a_b(0) = a_b(z_t) = 0$, implies $\bar{a}_b = 0$. Meanwhile, mass continuity implies $\bar{p} \partial \bar{w} / \partial t = 0$. Applying these results to the horizontal average of (B8) yields

$$\begin{aligned}
 -\partial_z \bar{p}_i &= \frac{1}{A} \iint dx dy \bar{\rho}(\mathbf{u} \cdot \mathbf{V})w \\
 &= \frac{1}{A} \iint dx dy \partial_i(\bar{\rho}u^i w) = \partial_z \overline{\rho w^2}.
 \end{aligned}$$

Integrating down from model top then shows that

$$\bar{p}_i = -\overline{\rho w^2}. \quad (\text{B9})$$

We can interpret this equation as follows. The quantity $\overline{\rho w^2}$ is simply the domain-averaged flux of vertical momentum $\overline{\rho w}$. The convergence ($-\partial_z \overline{\rho w^2}$) of this flux is a force—namely, the rate at which inertial motions generate $\overline{\rho w}$. Continuity dictates that $\overline{\rho w} \equiv 0$, however, and so (B9) just says that \bar{p}_i provides the force necessary to ensure this, in consonance with our discussion in the last section.

As a final note, (B9) and the Dirichlet BCs on w show that \bar{p}_i obeys both Neumann and Dirichlet BCs, and so either (or a mix) may be used in practice. Also, the relation in (B9) serves as a useful diagnostic constraint against which one may check their calculation of p_i .

REFERENCES

- Arakawa, A., and V. R. Lamb, 1977: Computational design of the basic dynamical processes of the UCLA general circulation model. *Methods Comput. Phys.*, **17**, 173–265, doi:10.1016/B978-0-12-460817-7.50009-4.
- Böing, S. J., H. J. J. Jonker, A. P. Siebesma, and W. W. Grabowski, 2012: Influence of the subcloud layer on the development of a deep convective ensemble. *J. Atmos. Sci.*, **69**, 2682–2698, doi:10.1175/JAS-D-11-0317.1.
- Bradshaw, P., and Y. Koh, 1981: A note on Poisson's equation for pressure in a turbulent flow. *Phys. Fluids*, **24**, 777–777, doi:10.1063/1.863442.
- Bretherton, C. S., J. R. McCaa, and H. Grenier, 2004: A new parameterization for shallow cumulus convection and its application to marine subtropical cloud-topped boundary layers. Part I: Description and 1D results. *Mon. Wea. Rev.*, **132**, 864–882, doi:10.1175/1520-0493(2004)132<0864:ANPFSF>2.0.CO;2.
- Das, P., 1979: A non-Archimedean approach to the equations of convection dynamics. *J. Atmos. Sci.*, **36**, 2183–2190, doi:10.1175/1520-0469(1979)036<2183:ANAATT>2.0.CO;2.
- Davies-Jones, R., 2003: An expression for effective buoyancy in surroundings with horizontal density gradients. *J. Atmos. Sci.*, **60**, 2922–2925, doi:10.1175/1520-0469(2003)060<2922:AEFEFI>2.0.CO;2.
- de Roode, S. R., A. P. Siebesma, H. J. Jonker, and Y. de Voogd, 2012: Parameterization of the vertical velocity equation for shallow cumulus clouds. *Mon. Wea. Rev.*, **140**, 2424–2436, doi:10.1175/MWR-D-11-00277.1.
- Doswell, C. A., and P. M. Markowski, 2004: Is buoyancy a relative quantity? *Mon. Wea. Rev.*, **132**, 853–863, doi:10.1175/1520-0493(2004)132<0853:IBARQ>2.0.CO;2.
- Droegemeier, K. K., and R. B. Wilhelmson, 1985: Three-dimensional numerical modeling of convection produced by interacting thunderstorm outflows. Part I: Control simulation and low-level moisture variations. *J. Atmos. Sci.*, **42**, 2381–240, doi:10.1175/1520-0469(1985)042<2381:TNDNOC>2.0.CO;2.
- Hacker, J., P. Linden, and S. Dalziel, 1996: Mixing in lock-release gravity currents. *Dyn. Atmos. Oceans*, **24**, 183–195, doi:10.1016/0377-0265(95)00443-2.
- Houze, R. A., Jr., 1994: *Cloud Dynamics*. International Geophysics Series, Vol. 53, Academic Press, 573 pp.
- Klemp, J. B., and R. Rotunno, 1983: A study of the tornadic region within a supercell thunderstorm. *J. Atmos. Sci.*, **40**, 359–377, doi:10.1175/1520-0469(1983)040<0359:ASOTTR>2.0.CO;2.
- Krueger, S. K., Q. Fu, K. Liou, and H.-N. S. Chin, 1995a: Improvements of an ice-phase microphysics parameterization for use in numerical simulations of tropical convection. *J. Appl. Meteor.*, **34**, 281–287, doi:10.1175/1520-0450-34.1.281.
- , G. T. McLean, and Q. Fu, 1995b: Numerical simulation of the stratus-to-cumulus transition in the subtropical marine boundary layer. Part II: Boundary-layer circulation. *J. Atmos. Sci.*, **52**, 2851–2868, doi:10.1175/1520-0469(1995)052<2851:NSOTST>2.0.CO;2.
- Kuang, Z., and C. S. Bretherton, 2006: A mass-flux scheme view of a high-resolution simulation of a transition from shallow to deep cumulus convection. *J. Atmos. Sci.*, **63**, 1895–1909, doi:10.1175/JAS3723.1.
- Lin, Y.-L., R. D. Farley, and H. D. Orville, 1983: Bulk parameterization of the snow field in a cloud model. *J. Climate Appl. Meteor.*, **22**, 1065–1092, doi:10.1175/1520-0450(1983)022<1065:BPOTSF>2.0.CO;2.
- List, R., and E. P. Lozowski, 1970: Pressure perturbations and buoyancy in convective clouds. *J. Atmos. Sci.*, **27**, 168–170, doi:10.1175/1520-0469(1970)027<0168:PPABIC>2.0.CO;2.
- Lord, S. J., H. E. Willoughby, and J. M. Piotrowicz, 1984: Role of a parameterized ice-phase microphysics in an axisymmetric, nonhydrostatic tropical cyclone model. *J. Atmos. Sci.*, **41**, 2836–2848, doi:10.1175/1520-0469(1984)041<2836:ROAPIP>2.0.CO;2.
- Mapes, B. E., 2000: Convective inhibition, subgrid-scale triggering energy, and stratiform instability in a toy tropical wave model. *J. Atmos. Sci.*, **57**, 1515–1535, doi:10.1175/1520-0469(2000)057<1515:CISSTE>2.0.CO;2.
- Margolin, L., W. Rider, and F. Grinstein, 2006: Modeling turbulent flow with implicit LES. *J. Turbul.*, **7**, doi:10.1080/14685240500331595.
- Markowski, P., and Y. Richardson, 2011: *Mesoscale Meteorology in Midlatitudes*. Vol. 2. Wiley-Blackwell, 430 pp.
- Mishra, S. K., 2011: Influence of convective adjustment time scale on the tropical transient activity. *Meteor. Atmos. Phys.*, **114**, 17–34, doi:10.1007/s00703-011-0154-8.
- , and J. Srinivasan, 2010: Sensitivity of the simulated precipitation to changes in convective relaxation time scale. *Ann. Geophys.*, **28**, 1827–1846, doi:10.5194/angeo-28-1827-2010.
- Mlawer, E. J., S. J. Taubman, P. D. Brown, M. J. Iacono, and S. A. Clough, 1997: Radiative transfer for inhomogeneous atmospheres: RRTM, a validated correlated-k model for the longwave. *J. Geophys. Res.*, **102**, 16 663–16 682, doi:10.1029/97JD00237.
- Neale, R. B., J. Richter, S. Park, P. H. Lauritzen, S. J. Vavrus, P. J. Rasch, and M. Zhang, 2013: The mean climate of the community atmosphere model (CAM4) in forced SST and fully coupled experiments. *J. Climate*, **26**, 5150–5168, doi:10.1175/JCLI-D-12-00236.1.
- Qian, Y., and Coauthors, 2015: Parametric sensitivity analysis of precipitation at global and local scales in the Community Atmosphere Model CAM5. *J. Adv. Model. Earth Syst.*, doi:10.1002/2014MS000354, in press.

- Rio, C., and Coauthors, 2013: Control of deep convection by subcloud lifting processes: The ALP closure in the LMDZ5B general circulation model. *Climate Dyn.*, **40**, 2271–2292, doi:[10.1007/s00382-012-1506-x](https://doi.org/10.1007/s00382-012-1506-x).
- Romps, D. M., 2008: The dry-entropy budget of a moist atmosphere. *J. Atmos. Sci.*, **65**, 3779–3799, doi:[10.1175/2008JAS2679.1](https://doi.org/10.1175/2008JAS2679.1).
- Rotunno, R., and J. Klemp, 1985: On the rotation and propagation of simulated supercell thunderstorms. *J. Atmos. Sci.*, **42**, 271–292, doi:[10.1175/1520-0469\(1985\)042<0271:OTRAPO>2.0.CO;2](https://doi.org/10.1175/1520-0469(1985)042<0271:OTRAPO>2.0.CO;2).
- Sherwood, S. C., D. Hernández-Deckers, M. Colin, and F. Robinson, 2013: Slippery thermals and the cumulus entrainment paradox. *J. Atmos. Sci.*, **70**, 2426–2442, doi:[10.1175/JAS-D-12-0220.1](https://doi.org/10.1175/JAS-D-12-0220.1).
- Siebesma, A. P., and Coauthors, 2003: A large eddy simulation intercomparison study of shallow cumulus convection. *J. Atmos. Sci.*, **60**, 1201–1219, doi:[10.1175/1520-0469\(2003\)60<1201:ALESIS>2.0.CO;2](https://doi.org/10.1175/1520-0469(2003)60<1201:ALESIS>2.0.CO;2).
- Tompkins, A. M., 2001: Organization of tropical convection in low vertical wind shears: The role of cold pools. *J. Atmos. Sci.*, **58**, 1650–1672, doi:[10.1175/1520-0469\(2001\)058<1650:OOTCIL>2.0.CO;2](https://doi.org/10.1175/1520-0469(2001)058<1650:OOTCIL>2.0.CO;2).
- Torri, G., Z. Kuang, and Y. Tian, 2015: Mechanisms for convection triggering by cold pools. *Geophys. Res. Lett.*, **42**, 1943–1950, doi:[10.1002/2015GL063227](https://doi.org/10.1002/2015GL063227).
- Wang, X., and M. Zhang, 2014: Vertical velocity in shallow convection for different plume types. *J. Adv. Model. Earth Syst.*, **6**, 478–489, doi:[10.1002/2014MS000318](https://doi.org/10.1002/2014MS000318).
- Weisman, M. L., and R. Rotunno, 2004: A theory for strong long-lived squall lines, revisited. *J. Atmos. Sci.*, **61**, 361–382, doi:[10.1175/1520-0469\(2004\)061<0361:ATFSLS>2.0.CO;2](https://doi.org/10.1175/1520-0469(2004)061<0361:ATFSLS>2.0.CO;2).
- Xu, K.-M., and D. A. Randall, 2001: Updraft and downdraft statistics of simulated tropical and midlatitude cumulus convection. *J. Atmos. Sci.*, **58**, 1630–1649, doi:[10.1175/1520-0469\(2001\)058<1630:UADSOS>2.0.CO;2](https://doi.org/10.1175/1520-0469(2001)058<1630:UADSOS>2.0.CO;2).
- Zhang, G. J., and N. A. McFarlane, 1995: Sensitivity of climate simulations to the parameterization of cumulus convection in the Canadian Climate Centre general circulation model. *Atmos.–Ocean*, **33**, 407–446, doi:[10.1080/07055900.1995.9649539](https://doi.org/10.1080/07055900.1995.9649539).